High-Resolution Imaging Without Iteration: A Fast and Robust Method for Breast Ultrasound Tomography

P. Huthwaite

Department of Mechanical Engineering

Imperial College London

SW7 2AZ,

UK

F. Simonetti

School of Aerospace Systems

University of Cincinnati

Cincinnati

OH 45221,

USA

(Dated: June 16, 2011)

Abstract

Breast ultrasound tomography has the potential to improve the cost, safety and reliability of breast cancer screening and diagnosis over the gold-standard of mammography. Vital to achieving this potential is the development of imaging algorithms to unravel the complex anatomy of the breast and its mechanical properties. The solution most commonly relied upon is Time-of-Flight Tomography but this exhibits low resolution due to the presence of diffraction effects. Iterative full-wave inversion methods present one solution to achieve higher resolution, but these are slow and are not guaranteed to converge to the correct solution. Presented here is HARBUT, the Hybrid Algorithm for Robust Breast Ultrasound Tomography, which utilises the complementary strengths of Time-of-Flight and Diffraction Tomography resulting in a direct, fast, robust and accurate high resolution method of reconstructing the sound-speed through the breast. The algorithm is shown to produce accurate reconstructions with realistic data from a complex 3D simulation, with masses as small as 4mm being clearly visible.

PACS numbers: 43.80Qf, 43.60Pt, 43.20Fn

I. INTRODUCTION

Breast cancer is by far the most common cancer among women throughout the world, with 411 000 deaths per year[1]. Breast cancer screening programmes, where women over the age of 40 to 50 years have their breasts regularly checked for cancer, have been shown to reduce death rates[2,3]. The current screening gold-standard is mammography, which projects X-rays through the breast so that the absorption of the photons by the structures within produces shadows which form an image. The detection of cancer is based on the assumption that the cancer mass is denser – and hence absorbs more X-ray radiation – than the surrounding tissue. The sensitivity (true positive rate) of the method is estimated at 68% to 88%[4], but this drops to around 30% to 40% in radiographically dense breasts where structures within the breast – parenchyma and stroma – mask the presence of cancer masses. Dense breast is a common occurrence, affecting approximately 50% of women under 50 years and a third over[5], and it is also in the latter group that the risk of developing cancer is the highest.

There are two main diagnostic tools complementary to mammography that are now routinely used in the clinic. The objective of these is to increase sensitivity and specificity (true negative rate). Magnetic Resonance Imaging (MRI) is one method, producing accurate images and achieving high sensitivity[6]. However, its use leads to a large number of unneeded biopsies due to its low specificity[7]. Additionally the cost of examination is typically an order of magnitude more expensive than mammography, and it relies on the injection of contrast agents, making it unsuitable for widespread screening.

A second option used to aid diagnosis is sonography, which produces an image via a handheld ultrasound array. Sonography is more sensitive in dense breasts than mammography because it can distinguish between structures with similar density but different acoustic impedance. However, being handheld, it is highly operator dependent and its use is limited to situations where the areas of interest – an ambiguous mass for example – have already been identified. This makes the technique in its current form unsuitable for screening.

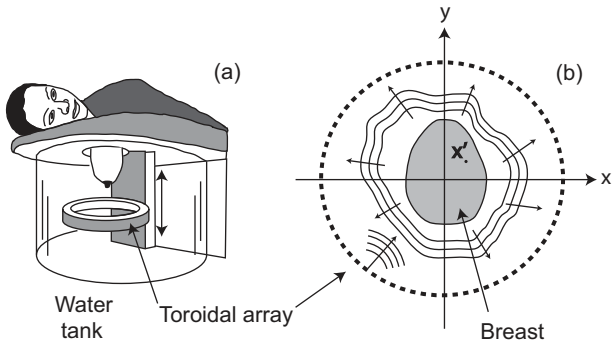

FIG. 1. Schematic of the system for breast ultrasound tomography. (a) The patient lies prone with the breast suspended in a water tank. A transducer array begins at the chest wall and gathers sets of data at many slices through the breast. Shown in (b) is a single illumination and the scattered field produced which is measured by the transducer array. We define $\mathbf{x}'$ as a point inside the scatterer.

The possibility of improving the sensitivity and specificity of sonography has been investigated since the 1970s within the framework of breast Ultrasound Tomography (UST)[8–15]. Thanks to recent progress in solid state electronics and array technology it is now possible to replace handheld probes with automated systems[11,12] such as the one shown in Fig. 1 which can produce full volume breast scans. The patient lies prone with the breast suspended in the water bath and the array is repeatedly moved down to image slices through it. At each slice, a single transducer provides an illumination, with the total field being recorded around the breast. This process is repeated with the next transducer providing the illumination and so on to provide a full matrix of scattering data for each vertical location of the array. This matrix is then used to reconstruct the mechanical properties of the materials within the breast with the goal of using these to distinguish cancer from healthy tissue. Identifying the characteristic mechanical properties of cancer within the breast is key to achieve high sensitivity and specificity. Greenleaf first proposed that cancer masses are characterised by higher sound speed and attenuation than the surrounding medium[16]; recent work is suggesting a similar pattern[12].

The dominant approach in breast UST is Time-of-Flight Tomography (TFT)[9,10,12,17–22]

which applies a ray-based approach to arrival times for transmitted signals in order to produce – either directly in the case of straight rays or with iterations for bent rays – a sound-speed map. This follows the approach in X-ray CT based reconstruction systems which can rely on simple straight ray approximations[23,24]. Diffraction effects are ignored under this approximation and a measure of the achievable resolution is $\sqrt{L\lambda}$ where L is the distance between transducer pairs and λ is the wavelength[25–31]. The size of a typical breast limits the shortest λ to about 1mm to achieve full breast penetration and the minimum distance between sensors L to about 200mm, thus resulting in a resolution in the region of 14mm. Although this should only be taken as an approximate estimation of the resolution of TFT, it suggests that TFT is not suitable for imaging very fine structures in the breast.

Higher resolution imaging methods based on the Born or Rytov approximations, such as Diffraction Tomography (DT)[32–35], are suitable for imaging fine details of the breast architecture. However, DT is of little use in breast imaging because the object to be imaged must be of low contrast relative to the background and small relative to λ, such that the maximum phase distortion through the object is much less than π, for the approximations to be valid. The breast is a large object (around 50λ across at $\lambda = 2$mm) and the contrast is high enough that the criterion for the validity of the approximation, as given in Ref. 34, cannot generally be satisfied for breast UST.

An alternative solution being considered is to improve the resolution of the TFT image with an iterative full-wave inversion technique[36–38]. The method uses the low resolution TFT algorithm to reconstruct a starting model of the breast mechanical properties. The algorithm then runs a numerical computer simulation to predict the signals that would be measured with the system in Fig. 1 for this model. The target of the algorithm is to minimise the residual between the resulting signal and the measured signal by updating the material properties of the breast; the breast model that minimises the residual provides the final image. The model refinement is generally achieved by a gradient-based stepping method. The first issue with this technique is that the algorithm will only converge to the nearest local minimum rather than the global minimum of the problem. Because of this, the starting

model – i.e. the image produced by the TFT algorithm – must already be close to the global minimum. Also, the technique is susceptible to uncertainties not considered in the forward model – for example transducer characteristics, 3D effects, and noise which can lead to the the algorithm converging to an incorrect solution. Speed is another significant drawback: a full set of illuminations needs to be simulated at each step (and more to calculate the gradient) with many iterations needed to generate the final image.

This paper introduces HARBUT, the Hybrid Algorithm for Robust Breast Ultrasound Tomography, which addresses the need for a fast, robust, high-resolution breast ultrasound tomography method, by combining the complementary strengths of the TFT and DT algorithms to reconstruct a sound speed map. The TFT image is used to correct for the aberration that causes DT to break down under the Born approximation. A similar approach has already been introduced by Mast[39], although this uses DT rather than TFT as a background, limiting the contrast which can be imaged. Here, we provide an imaging algorithm optimised for the circular array configuration in Fig. 1, and study how 3D features close to the image plane affect the reconstructions. The latter point is of primary importance because the circular array configuration is not ideal for 3D imaging which would require a spherical aperture.

Sec. II describes the standard Born approximation upon which DT is based and modifies it such that it forms the basis for the new algorithm. Sec. III presents the new imaging method, and Sec. IV details the model and data that will be used to test it. Sec. V presents the image reconstructions obtained with the new method and consideration to practical implementation is given in Sec. VI.

II. SCATTERING THEORY

Here, we introduce a formulation for ultrasound scattering that provides the basis for the imaging method presented in Sec. III.

The standard acoustic wave equation[40] is the accepted model used to describe ultrasound

propagation in tissue

$$\rho(\mathbf{r})\nabla.\left[\frac{1}{\rho(\mathbf{r})}\nabla p(\mathbf{r})\right]-\frac{1}{c(\mathbf{r})^2}\frac{\partial^2 p(\mathbf{r})}{\partial t^2}=0 \tag{1}$$

where $p(\mathbf{r})$ is the pressure at point $\mathbf{r}$, $\rho(\mathbf{r})$ is the density and $c(\mathbf{r})$ is the sound speed. By converting this to the temporal frequency domain it can be rewritten as

$$(\nabla^2+k_w^2)\psi=-O\psi \tag{2}$$

where ψ is the scalar potential of the field (equal to the Fourier transform of the pressure) and $k_w=2\pi f/c_w$ is the wavenumber of the water background where f is the frequency and c_w is the sound speed in water. Throughout this paper the homogeneous background corresponds to the water bath (with subscript w), although these equations are valid for any homogeneous background. The object function, $O(\mathbf{r})$, is the mathematical representation of the breast and is defined as

$$O(\mathbf{r})=k_w^2\left[\left(\frac{c_w}{c(\mathbf{r})}\right)^2-1\right]-\rho^{1/2}(\mathbf{r})\nabla^2\rho^{-1/2}(\mathbf{r}) \tag{3}$$

where $c(\mathbf{r})$ is the actual sound speed at point $\mathbf{r}$. The aim of tomography is to reconstruct this object function. The second term in (3) accounts for variations in the local density field, ρ[41]. The dependence of the density term on the Laplacian means that it is only significant at an interface where rapid changes in density occur; this term will therefore be low away from the boundaries within the breast and is considered negligible for the rest of this paper, as will be explained in detail later in Sec. VI.

In order to solve (2) we define the water wave field ψ_w as the solution to the case where there is no breast immersed in the water, and use the Green's function in water G_w to reach, under the Born approximation[33,34]

$$\psi\approx\psi_w-\int_\Omega G_w O\psi_w d\mathbf{x}'. \tag{4}$$

For the Born approximation to be valid, the maximum phase distortion as waves pass through the object must be less than π[34]. It is this that limits the applicability of the stan-

dard Born approximation imaging methods to breast UST – the breast is typically around 100mm (50λ at $\lambda = 2mm$) in diameter meaning that its sound speed contrast relative to the water bath must be less than 1% to meet this criterion.

In this paper we address the phase distortion problem by dividing the object function into a sum of an 'artificial' inhomogeneous background object function O_b, and a small perturbation O_δ so that

$$O(\mathbf{r}) = O_b(\mathbf{r}) + O_\delta(\mathbf{r}). \tag{5}$$

Using the same procedure as in standard DT[33,34] we can derive the following integral

$$\psi = \psi_b - \int_\Omega G_b O_\delta \psi d\mathbf{x}' \tag{6}$$

where G_b is the Green's function defined for the inhomogenous background and ψ_b is the illumination distorted by the background.

Provided O_δ is sufficiently small, under the integral we can approximate the ψ term with the background term ψ_b so that

$$\psi \approx \psi_b - \int_\Omega G_b O_\delta \psi_b d\mathbf{x}' \tag{7}$$

which is a more accurate version of (4). Equation (7) is central to the Distorted Born Iterative Method (DBIM) that aims to solve the wave equation through an iterative scheme[42]. For (7) to be sufficiently accurate the background medium has to be selected so as to ensure that the phase difference between ψ_b and ψ is much less than π. This is the inhomogeneous equivalent of the standard Born criterion as given in Ref. 34.

It is the combination of size and contrast of the bulk of the breast which breaks the standard Born approximation. Provided we have a background that accounts for the average speed through the breast then the sizes and contrast of the remaining perturbations should be small enough that the Born approximation criterion given in Ref. 34 will be valid for them. In this context, TFT provides a suitable background, as will be demonstrated in Sec. V.

III. THE HARBUT METHOD

This section uses the formulation from the previous section as a basis for HARBUT. We start from a particular implementation of DT that has been introduced in Ref. 43.

A. An implementation of DT

This method consists of two main steps: beamforming (BF) and the application of a filter. We begin with the derivation of the beamforming algorithm.

We introduce the coordinates $\mathbf{x}$ and $\mathbf{y}$ as the coordinates of the receiver transducer and source transducer respectively. $\mathbf{x}'$ is defined as in Fig. 1. Using these, and defining the scattered field as $\psi_s = \psi - \psi_w$, we can rewrite (4) as

$$\psi_s(\mathbf{x}, \mathbf{y}) \approx -\int_\Omega G_w(\mathbf{x}, \mathbf{x}') O(\mathbf{x}') \psi_w(\mathbf{y}, \mathbf{x}') d\mathbf{x}'. \tag{8}$$

We can demonstrate the symmetry of this equation by recognising that $\psi_w(\mathbf{y}, \mathbf{x}') = G_w(\mathbf{y}, \mathbf{x}')$ i.e. the field produced by an illumination at $\mathbf{y}$ can simply be replaced by the equivalent Green's function. This leads to

$$\psi_s(\mathbf{x}, \mathbf{y}) \approx -\int_\Omega G_w(\mathbf{x}, \mathbf{x}') O(\mathbf{x}') G_w(\mathbf{y}, \mathbf{x}') d\mathbf{x}'. \tag{9}$$

Now consider a single point scatterer in a water background. In this case, the equation is simplified from an integral to

$$\psi_s(\mathbf{x}, \mathbf{y}) = G_w(\mathbf{x}, \mathbf{x}') q G_w(\mathbf{x}', \mathbf{y}) \tag{10}$$

where we have taken the scattering potential of the point as q, located at $\mathbf{x}'$. Knowing the location of the point scatterer we can rearrange (10) to determine the exact scattering potential from a single scattering measurement, i.e.

$$q = \frac{\psi_s(\mathbf{x}, \mathbf{y})}{G_w(\mathbf{x}, \mathbf{x}') G_w(\mathbf{x}', \mathbf{y})}. \tag{11}$$

In this equation, it can be considered that the $\frac{1}{G_w}$ factors provide corrections to the scattered field ψ_s so as to account for the phase shift and amplitude change as the wave propagates through the medium. In general, however, the location of each scatterer is unknown, and there are multiple scatterers present so that the signals interfere and make the use of (11) unfeasible in its current form.

The solution considered here is to take advantage of the multiple send-receive pairs in the data, rather than just the single pair as above. This is done in the beamforming algorithm (also known as the sum and delay method or SAFT - Synthetic Aperture Focusing Technique), which is performed in the time domain by applying a backwards time shift to account for the shift that occurs as the wave propagates through the medium, and summing up the results for each send-receive pair[44–46]. In the frequency domain, the time-shifts correspond to the phase shifts of the Green's functions, so that the image value at point $\mathbf{z}$ is

$$I^{BF*}(\mathbf{z}) = \int_{\mathbb{S}}\int_{\mathbb{S}} \frac{\psi_s(\mathbf{x},\mathbf{y})}{\operatorname{sgn}\left[G_w(\mathbf{x},\mathbf{z})\right]\operatorname{sgn}\left[G_w(\mathbf{z},\mathbf{y})\right]} d\mathbf{x}d\mathbf{y} \tag{12}$$

where $\mathbb{S}$ is the aperture of the transducer array and the sign function is defined as $\operatorname{sgn}(x) = {}^{x}/_{|x|}$ so that only the phase component of G_w is used. For real, sampled data the continuous integrals are replaced by discrete sums. Due to this integral/summing process, if there is a scatterer present at the imaging point then the integrand will sum coherently leading to a large value, but if there is no scatterer at the point then the summing will be incoherent and the result will be much weaker, with the values cancelling themselves out.

When quantitatively determining the scattering potential in Eq. (11), it is clearly necessary to correct for both amplitude and phase changing as the wave travels through the medium. Following this, we adjust Eq. (12) to use the full Green's functions in the beamforming integrand, matching the form of Eq. (11), to give

$$I^{BF}(\mathbf{z}) = \int_{\mathbb{S}}\int_{\mathbb{S}} \frac{\psi_s(\mathbf{x},\mathbf{y})}{G_w(\mathbf{x},\mathbf{z})G_w(\mathbf{z},\mathbf{y})} d\mathbf{x}d\mathbf{y}. \tag{13}$$

Throughout this paper we use this version of the BF algorithm since by accounting for amplitude we keep the algorithm more general. This would allow us, for example, to ac-

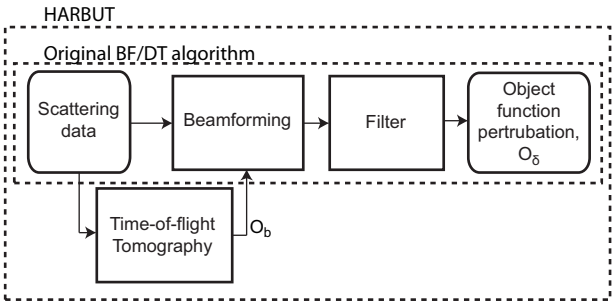

FIG. 2. Flowchart of the stages which make up the original BF/DT algorithm, and the additional TFT stage which is included in HARBUT

count for background media which cause significant amplitude changes, for example through attenuation.

As discussed in Ref. 43, the BF image is a distorted image of the DT reconstruction with different weights applied to different spatial frequencies which generates a distorted reconstruction. The DT reconstruction is obtained by correcting this weighting, which is done by Fourier transforming the BF image, applying the weighting corrections, and transforming the result back to the geometrical space. This approach is more flexible than directly generating the DT image, and is essential for HARBUT, as presented in the next section.

B. Combining DT and TFT

We now consider the case of imaging in an inhomogeneous background. This process is similar to the homogeneous case, with the addition of the TFT algorithm to provide a suitable background. Fig. 2 illustrates the process.

The first step is to perform the beamforming algorithm, this time accounting for the background. Starting from (7), we substitute $\psi_b = G_b$ and include the source and receiver coordinates $\mathbf{x}$ and $\mathbf{y}$

$$\psi(\mathbf{x},\mathbf{y}) \approx \psi_b(\mathbf{x},\mathbf{y}) - \int_\Omega G_b(\mathbf{x},\mathbf{x}')O_\delta(\mathbf{x}')G_b(\mathbf{y},\mathbf{x}')d\mathbf{x}'. \tag{14}$$

We use a TFT image to provide the background sound speed field. In this paper we generate the TFT image by the method in Ref. 47, although the actual method used is not critical to the success of the algorithm, provided it gives a reasonable low resolution reconstruction of the sound-speed. The Green's functions for this background field need to be calculated via a numerical simulation, where each illumination is calculated separately to provide wavefield values at all points in the imaging domain. An eikonal equation solver[48] provides sufficiently accurate results throughout the domain, with significant speed advantages over alternatives such as frequency domain finite difference; a secondary advantage of using ray-approximation-based methods is that such solvers (and the solutions they provide) are often already available as part of the TFT algorithm. The use of the eikonal solver is a distinction between our algorithm and Ref. 39, which uses a simple straight-ray approximation; our algorithm is therefore better suited to cases where the breast causes significant refraction. The numerical method is only used to provide a phase correction relative to the Green's function in homogeneous water bath, so that

$$G_b\left(\mathbf{x}', \mathbf{y}\right) = G_0\left(\mathbf{x}', \mathbf{y}\right) e^{i\omega\Delta t} \tag{15}$$

where Δt is the difference in arrival time between the propagation in the background model and propagation in homogeneous water, calculated via the eikonal solver.

If we now consider a point scatterer in an inhomogeneous medium, we can follow through exactly the same logic as in Sec. III.A except starting with (14) instead of (9) to give the BF image of the perturbation relative to the background,

$$I_\delta^{BF}(\mathbf{z}) = \int_{\mathbb{S}}\int_{\mathbb{S}} \frac{\psi_\delta(\mathbf{x}, \mathbf{y})}{G_b(\mathbf{x}, \mathbf{z}) G_b(\mathbf{z}, \mathbf{y})} d\mathbf{x} d\mathbf{y} \tag{16}$$

where $\psi_\delta = \psi - \psi_b$ is the perturbation of the measured field relative to the background. Given that all of these quantities can be established, either from measurements or numerical models, we can form the modified beamforming image from this equation. This is similar in approach to the Kirchhoff migration method used in geophysics[49]. Kirchhoff migration is only used on reflected data, however, and reconstructs the interfaces of impedance variations

in the subsurface rather than material properties. Similar work has been done in medical imaging which again only reconstructs impedance variations[13].

The BF image generated from (16) is then converted to the DT image using the filter introduced in Ref. 43. This filter is given as a function of spatial frequency, $\mathbf{\Omega}$ as

$$F(\mathbf{\Omega}) = \frac{k_w|\mathbf{\Omega}|\sqrt{1-|\mathbf{\Omega}|^2/4k_w^2}}{8\pi^2\Pi}\Lambda(\mathbf{\Omega}) \tag{17}$$

where

$$\Lambda\left(\mathbf{\Omega}\right) = \begin{cases} 1, & |\mathbf{\Omega}| < 2k_w \\ 0, & |\mathbf{\Omega}| > 2k_w. \end{cases}$$

Having obtained O_δ by filtering I_δ^{BF}, it is combined with the background velocity field according to (3) and (5), forming the final HARBUT image. It should be observed that HARBUT solves (7); this process corresponds to the first iteration of the DBIM[42,50]. However, our approach uses a different scheme to solve (7) based on the TFT starting model and the combination of BF and DT. This combination represents the main novelty of the method and is key to its robustness and speed, as discussed next.

Mast[39,51] proposed a similar synthetic-aperture type method for reconstructing sound speed maps while correcting for aberrations. However, this was only used for iterating from a homogeneous starting point, rather than a TFT image, so its range of validity was only about double that of the standard Born approximation. The contrast and size of the breast – in general – is likely to be beyond this.

For the proposed method to be feasible in practice, it is necessary to consider the experimental constraints that affect the nature and accuracy of the measurements. In this context, the main factors are:

1. 3D effects and sampling conditions. The array architecture shown in Fig. 1 is suitable for imaging 2D objects. The anatomy of the breast is fully 3D which would require a spherical array to perform all the measurements required to satisfy the Nyquist sampling criterion. Therefore it is important to understand whether the reconstruction can be treated as 2D and what type of artefacts one could expect as a result.

2. Knowledge of ψ_b. In order to form the BF image with (16), the scattered field $\psi_\delta = \psi - \psi_b$ needs to be known. Although ψ is directly available from the measurements, ψ_b cannot be measured. It would therefore be necessary to use a forward solver that predicts the outcome of the measurements that would be taken if only the background medium was present. However, for the calculations to be sufficiently accurate, one would need a very accurate model of transducer response and to be able to account for 3D effects. This challenge is magnified because $|\psi_\delta| \ll \{|\psi|, |\psi_b|\}$, meaning that even small errors in the estimate of ψ_b would lead to large errors in ψ_δ. Therefore, it is critical to understand whether ψ could be used in (16) instead of ψ_δ.

3. Density. Once the object function has been reconstructed, the sound speed and density have to be obtained by inverting (3). However, $O(\mathbf{r})$ at a single frequency does not contain sufficient information to extract both material properties. As a result, it is important to understand if the density term in (16) can be neglected to obtain sound speed only.

4. Attenuative effects. As the incident wave travels through the breast, its amplitude will be reduced due to the attenuative properties of human tissue. It is important to understand the effect this has on the resulting image and whether it can be accounted for by the algorithm.

Sections V and VI show how the proposed method addresses these points.

IV. FORWARD MODEL

This section details a numerical model used to test HARBUT, as introduced in Sec. III. The aim is to demonstrate the robustness of the new algorithm by generating data which reproduces realistic experimental conditions.

Such data is provided by a 3D model solved numerically with the Finite Difference Time Domain (FDTD) method. This models sound speed and density in 3D, as well as accounting for the size of the transducers in the z direction.

A. Physical model

Selecting a suitable, realistic breast model is challenging since the necessary material properties of the breast are difficult to measure and tend to vary from person to person. The wide range in quoted values (see for example Refs. 52–54) reflects this variation. Therefore, we use the more extreme, higher contrast values (which are more challenging to Born-approximation-based algorithms) in order provide a thorough test of the new algorithm.

The model is fully 3D to represent the actual shape of the human breast, as shown in Fig. 3 for the sound speed and density. A glandular region forms the bulk of the breast model, with an irregular subcutaneous fat layer around the boundary. Material properties for the glandular region and fat are given in Table I. Existing numerical studies have so far used data generated by 2D models used to test breast UST algorithms; a novel aspect of our work is the use of more realistic 3D data for this purpose.

The glandular region is represented by a random medium. As shown in Refs. 55, 56, a random medium will reduce the amplitude of a transmitted signal by diverting energy away from the receivers and out of the plane of the array, thus leading to a form of apparent attenuation. The same effect is produced by the small scale features in the breast which are also responsible for the speckle phenomenon. We use a random medium model based on that outlined in Ref. 54, although with longer correlation lengths due to the relatively large spacing of the FDTD grid. Following the empirical relationship that density tends to vary linearly with sound speed[57], we use the same random field pattern for both density and velocity.

Five inclusions are placed in the model: three representing cancer masses and two representing fat spheres. The material properties of these are given in Table I and the dimensions and locations in Table II. The goal of the imaging algorithm is to be able to detect these and identify whether each inclusion is cancer from the reconstructed mechanical properties.

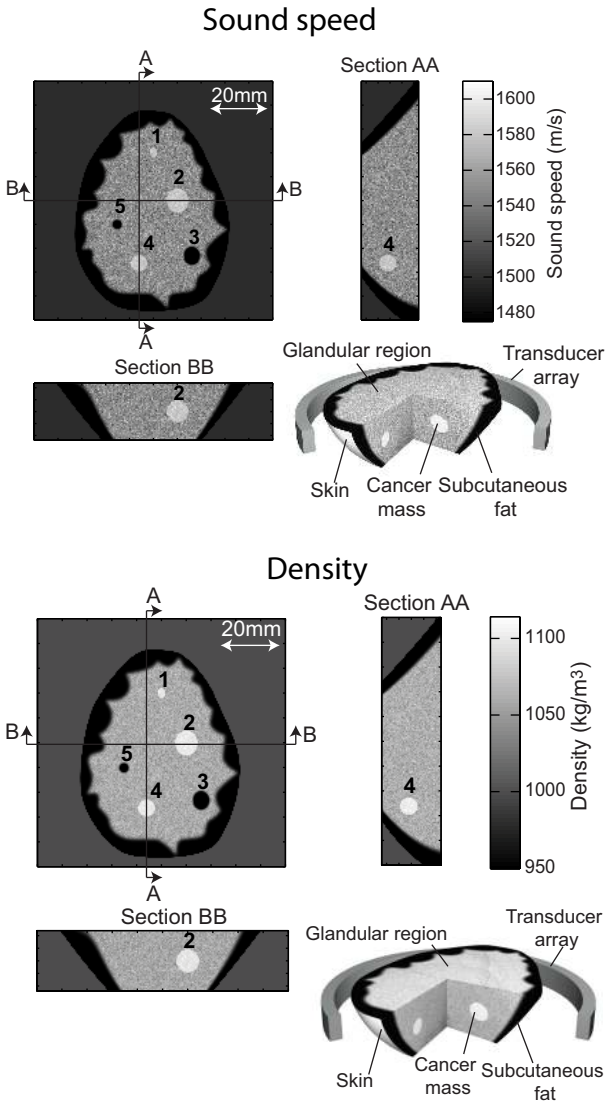

FIG. 3. 3D numerical model of a breast with non-uniform sound speed and density

B. Array model

A 450 transducer array (sufficient elements according to the sampling criterion in Ref. 58) is considered. The transducers are 12mm tall (in the z direction) but thin within the plane of the array so as to act as line sources. The array has a diameter of 120mm to limit the size of the propagation domain and hence the computational burden of the 3D model. Each array element is excited with a 3-cycle Hann windowed toneburst at a centre frequency of 750kHz. This has a bandwidth of 250 to 1250kHz.

C. Numerical simulation

A 3D FDTD modelling method is used with a standard Yee grid[59], with the mesh terminated with efficient convolutional perfectly matched layers[60] to minimise reflections from the boundary of the domain. 14 nodes were used per 2mm wavelength, so that the grid spacing is 1/7 mm. A domain of 861 by 861 by 189 nodes was used. This is large enough for the 120mm array in the x and y directions and is 24mm tall in the z direction to allow the beam to diffract as it travels into the domain. A Courant number of 0.95 is chosen which gives a time step of 2.96×10^{-8}s (based on a maximum velocity of 1620m/s), therefore needing 4056 time steps for the 0.12ms simulation (long enough for a wave in water to travel 1.5 times the array diameter). The array locations are rounded to the nearest node so the recorded coordinates for each transducer are adjusted accordingly. 450 separate simulations have to be performed – one for each illumination. To model the effect of the transducer out of the plane, each transducer is modelled as a set of in-phase point sources at all nodes along a 12mm tall line.

A single illumination for this configuration takes around 4 hours to run on a single core of an AMD Opteron 8384 2.7GHz processor. Parallelism was achieved in a coarse-grained manner by running many – typically 64 – illuminations simultaneously. Using a cluster of two quad-core Intel Xeon E5462 2.8GHz processors per node and 40 nodes, running all 450 simulations was completed within around 48 hours, with quite a large dependency on the queueing system in place on the cluster. These times are for the forward simulation only; the actual imaging algorithm, running on a single computer, is several orders of magnitude faster, as detailed in Sec. V.

D. Data Processing

Two sets of data are generated: an incident data set where the material properties throughout the model are the same as that of water and the set for the case where the breast phantom described in Sec. IV.A is present. When performing experimental measurements,

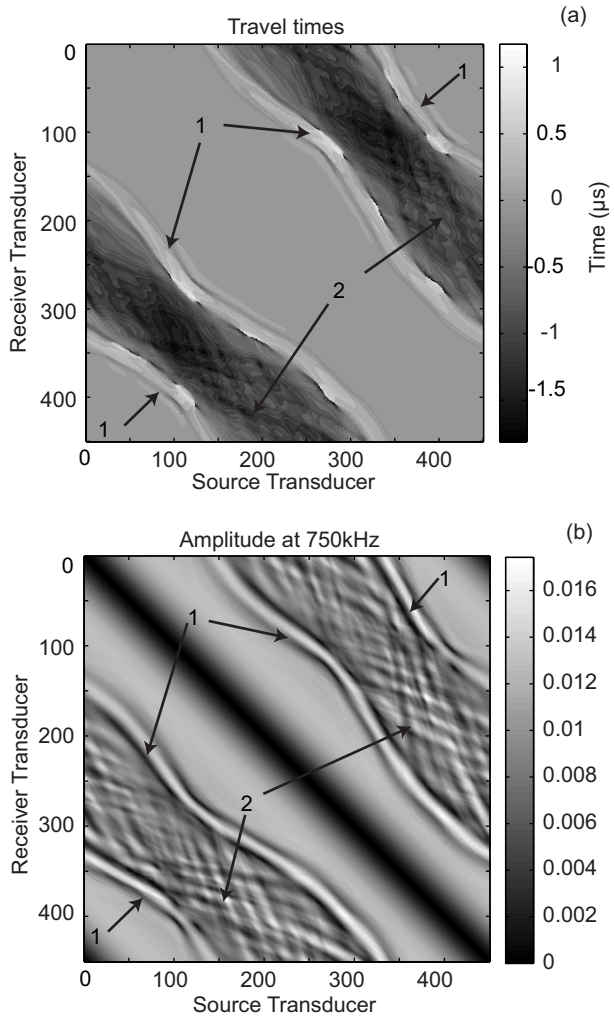

FIG. 4. Matrices of processed data, plotted for all send-receive pairs. (a) gives the arrival times of the modelled signals relative to the incident signal, estimated by a frequency domain deconvolution. (b) presents the amplitude, taken at 750kHz. In both plots, the regions marked 1 correspond to the transmit-receive pairs with a line-of-sight passing through the subcutaneous fat layer and those marked 2 to the transducer pairs that 'see through' the volume of the phantom.

the incident data set can be generated by taking measurements when there are no objects present in the water bath. These data need to be processed prior to passing them through the imaging algorithms.

Fig. 4(a) presents this difference in arrival times, estimated for all send-receive pairs

relative to the incident field. The arrival time is defined as the time at which the first disturbance is measured at the receiver. These have to be established quantitatively in order to be able to perform the TFT algorithm; here we use a deconvolution via the frequency domain. The aim of this deconvolution is to find what the incident signal is convolved with to generate the total, time-shifted signal; ideally this forms the Dirac delta function, the offset of which provides the relative time offset. We perform the deconvolution by Fourier transforming the total signal and dividing by the Fourier transform of the incident signal, then inverse Fourier transforming the result back to the time domain. The relative arrival time is taken as the peak of the resulting function. Following the Wiener Deconvolution[61] we add an extra term to the denominator of the division to avoid division by zeros. There are more accurate methods (e.g. Ref. 62) of establishing the arrival times but this is sufficiently accurate for us to obtain the low resolution TFT background we need. In the figure, the regions marked as 2 correspond to the send-receive pairs with a line of sight through the glandular region of the model; the main effect is to make the waves arrive earlier due to the higher sound speed of the glandular material. To either side of these diagonal regions, in the boundaries marked 1, the waves do not pass into the glandular region but only pass through the subcutaneous fat, which is slower than the water bath and leads to later arrival of the waves. These therefore appear lighter in the figure.

Fig. 4(b) gives the amplitude of each send-receive pair, produced at 750kHz by taking a discrete Fourier transform of the measured data. The data have been normalised such that they represent what would be seen if a unit point source was used to provide the illumination. If there was no scatterer present then the field would be the same as the Green's function sampled around the array. Under this condition, a singularity would be present along the principal diagonal due to the measurement being taken at the source location. However, this singularity is removed by gating off the incident signal for the source and surrounding measurements, which leaves the dark stripe down the diagonal.

The bright boundaries (marked 1) are the waves which have passed solely through the subcutaneous fat. The relatively high amplitude indicates that some form of focusing is

occurring. Waves passing through the bulk of the glandular region, 2, have lower amplitude due to the effects of the random glandular material that scatters sound in all directions in space. The diagonal crossing patterns throughout this region are due to the presence of the inclusions.

V. RESULTS

Fig. 5 shows the separate stages of HARBUT compared to the original sound speed model of the central slice of the phantom in Fig. 5(a). The TFT reconstruction in Fig. 5(b) shows the expected low resolution characteristics since diffraction is not accounted for. The reconstruction allows us to detect the subcutaneous fat layer and the glandular region; however, the inclusions are not reliably detectable. Enhanced TFT reconstructions are likely to be possible – for example by using a higher centre frequency to improve resolution – but the improvements will still be fundamentally limited by the algorithm's inability to deal with diffraction.

Fig. 5(c) is the modified BF image using the background from Fig. 5(b). The absolute value of the complex values at each pixel is plotted. In this reconstruction, the total field ψ is used rather than the perturbation ψ_δ. The features are masked by the presence of the transmission signals in the data used to reconstruct the image. Converting to the DT image in Fig. 5(d), using the filter from Ref. 43 based on the free space k_w, allows all five inclusions to be identified. The inclusions appear inverted because of the definition of the object function in eq. (3). This perturbation component is sufficiently small that the approximation $\psi = \psi_b$ necessary for the algorithm to work is valid. The total object function in Fig. 5(e) is calculated by combining O_b from Fig. 5(b) and the O_δ in Fig. 5(d) according to (5).

Fig. 5(f) is the final sound speed reconstruction obtained from Fig. 5(e) by inverting (3) and ignoring density effects. All five inclusions can be very clearly seen and all the irregular features of the subcutaneous fat layer are reconstructed. The sharp boundaries at the edge

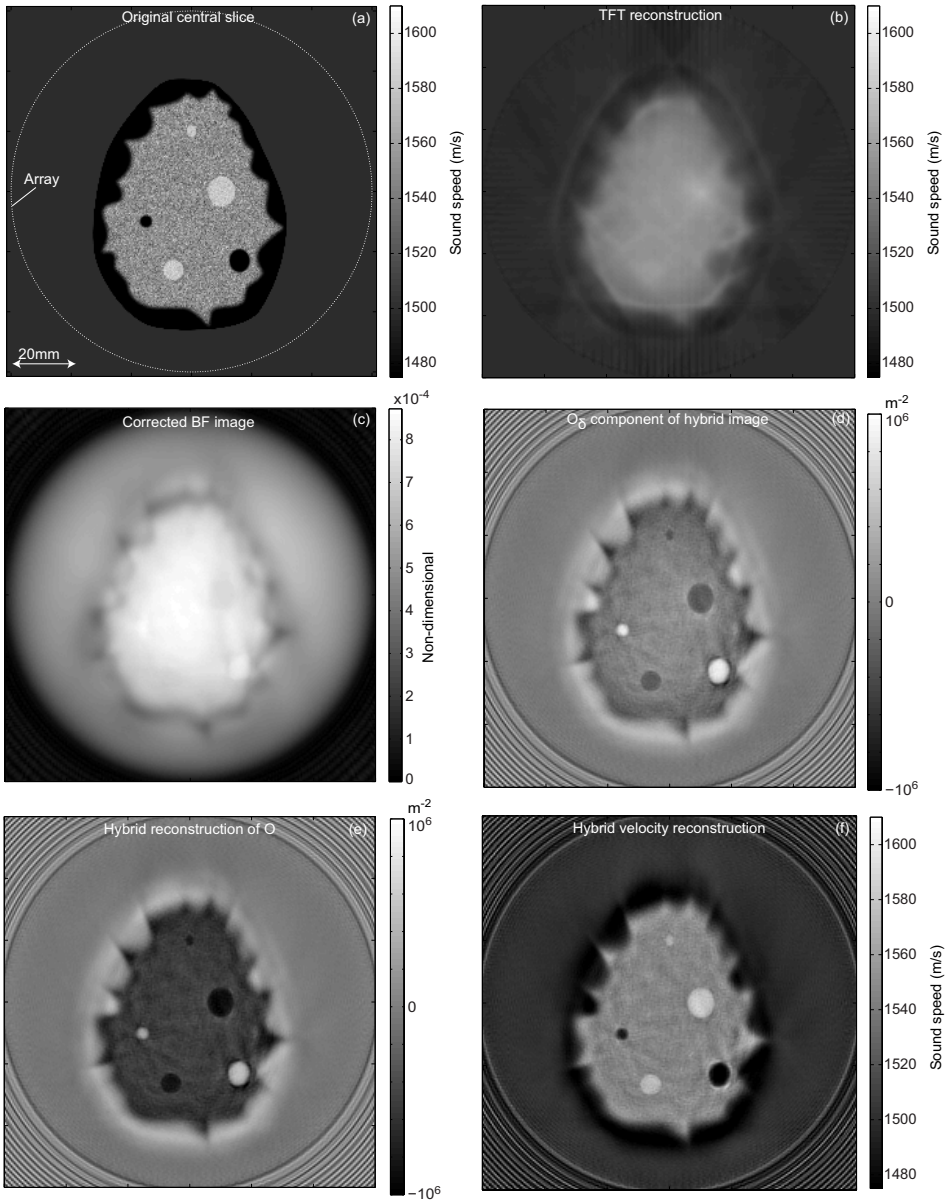

FIG. 5. (a) The original central slice of the sound speed map as in Fig. 3, with the locations of the transducer array marked. (b) is the TFT sound speed reconstruction. This is used as the background for the corrected beamforming at 750kHz in (c). The modulus of the complex reconstruction is given. This is then filtered to get the object function perturbation component O_δ given in (d). (e) is the full object function O generated by combining (d) and the background object function O_b calculated from (b). (f) is the hybrid sound speed reconstruction from the object function (e).

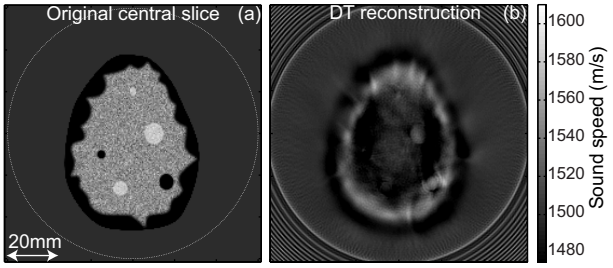

FIG. 6. Standard DT reconstruction. The size and the contrast of the original phantom (a) are large enough that the standard Born approximation is invalid, causing the reconstruction (b) to have extensive artefacts that obscure the inclusions.

of the model and at the edge of the glandular region are blurred in the reconstruction; also the random medium representing the glandular region appears more homogeneous. This blurring is due to an averaging effect in the z direction that determines the so called slice thickness[63] as discussed in Sec. VI. This effect is also responsible for the reconstructed contrast of inclusion 1 being reduced.

In Tab. III we present the average sound speeds through each of the reconstructed inclusions. Due to the z-direction averaging, the contrast tends to be reduced, particularly for the smaller inclusions. Overall, however, all inclusions are reconstructed with a small error – within 0.72% – and the image is a dramatic improvement over the TFT reconstruction of Fig. 5(b).

The use of beamforming before the application of the DT filter makes HARBUT very robust against noise. We have tested how HARBUT performs when noise is present by adding a noise matrix, N, to the matrix in Fig. 4(b). The entries of the N-matrix are complex random numbers with a Gaussian amplitude distribution with standard deviation s and phase uniformly distributed between $-\pi$ and π. The noise level is defined as the ratio between s and the rms value of the moduli of the entries in the matrix in Fig. 4(b). The sound speed reconstruction with the noise present has a slightly granular appearance, but apart from this is effectively unchanged.

Finally, to demonstrate the effectiveness of HARBUT, Fig. 6(b) shows the reconstruction

obtained with the standard BF/DT algorithm[43] with a homogeneous water background. Due to the size and contrast of the phantom relative to the water background, the condition for validity of the Born approximation is violated. As the illuminating field travels inside the phantom, it accumulates a phase delay larger than π. As a result, the total field that propagetes through the object is in opposition of phase with the free space incident field (which replaces it under the Born approximation) leading to the artefacts in Fig. 6(b).

The current implementation of the BF/DT stage uses Matlab. To generate the 481 by 481 pixel image given the background correction data currently takes around 60 seconds on an HP z600 dual quad-core workstation without significant optimisation. The background correction data, required to calculate G_b, are taken from the final iteration of the TFT algorithm and therefore have no associated overhead. We have also produced an optimised C++ version which produces the same image in 5 seconds. This compares to the TFT method itself which takes around 1 minute to complete (although this is strongly dependent on parameters such as pixel size) and DBIM which according to one example, where it is applied to breast ultrasound tomography[50], took around 9 hours per iteration for a relatively small domain of 50λ by 50λ.

VI. PRACTICAL CONSIDERATIONS

In this section we discuss the practical aspects that were introduced at the end of Sec. III, points 1) to 4).

A. 3D effects and sampling conditions

Fig. 7 compares the hybrid image from the 3D data as in Fig. 5(f) with a reconstruction using data from a similar simulation, except performed in 2D using the central slice of Fig. 3. The 2D reconstruction has sharp boundaries at the edge of the glandular region and the breast itself, which are both blurred in the 3D version. The granular appearance of the random medium is also better defined in the 2D reconstruction than the 3D. These

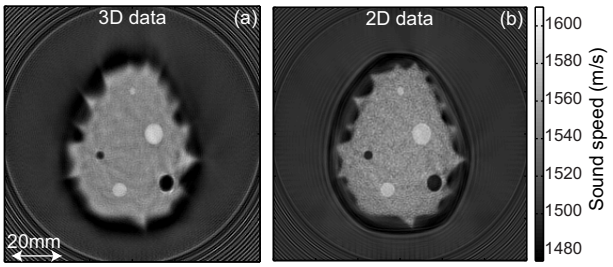

FIG. 7. Comparison of the HARBUT reconstruction from 3D data (a) and 2D data (b). The boundaries of the glandular region and the phantom itself in the 3D reconstruction are blurred in comparison to the 2D reconstruction. The random medium which makes up the glandular region is also more homogeneous in the 3D reconstruction. These effects are a result of averaging in the out-of-plane direction.

differences are caused by blurring in the z (out-of-plane) direction in the 3D reconstruction due to the finite height of the transducer beam, as will be explained in this section.

For this purpose it is necessary to consider the 3D Point Spread Function (PSF) which gives the response of the imaging system to a point scatterer. If the PSF is space invariant, i.e. does not depend on the position of the point scatterer, then the image is a convolution of the PSF with the original object function. The PSF is space invariant for standard DT[43], assuming plane wave illuminations and measurements taken in the far field, and here we assume that it can also be considered space invariant for HARBUT due to the relatively low contrast of the background sound speed map.

To generate the 3D PSF, a point scatterer at the origin – the centre of the array at $z = 0$ – is imaged with the transducer array at several axial locations; these images are then stacked to form the point scatterer response. Fig. 8 gives the PSF for the system considered in this paper. In the x and y directions it is 1mm ($\lambda/2$) thick because of the Born approximation resolution limit, but in the z direction – as shown in Fig. 8(d) – the response stretches out to around $\pm$4.5mm, using a threshold of $-$6dB relative to the maximum.

Due to the convolution, each point in the final image will be a weighted average of the object function in the z direction with the weights defined by the PSF projection in Fig. 8.

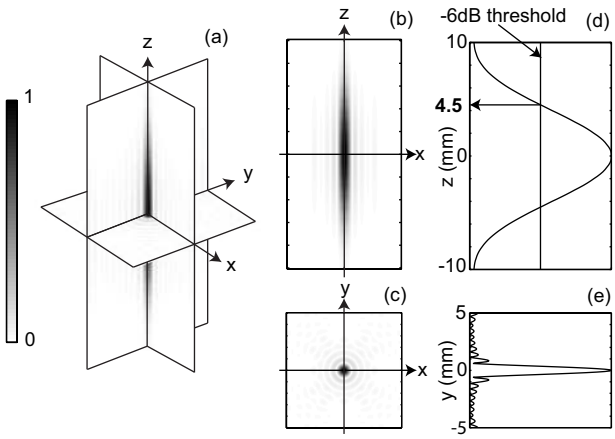

FIG. 8. Normalised Point Spread Function at the centre of the array for the system modelled in this paper – 12mm tall transducers with an array diameter of 120mm. The PSF is thin – about 1mm ($\lambda/2$) wide – within the plane due to the resolution of the Born approximation used in the reconstruction. As shown in (d), taking a threshold at -6dB relative to the maximum, the PSF extends in the region $-4.5\text{mm} < z < 4.5\text{mm}$, making its height around 9mm. This is significantly wider than the in-plane PSF dimensions.

This means that any structure not aligned in the z direction will be blurred in the final reconstruction. This is evident in Fig. 5(f), where the boundaries of the glandular region and the subcutaneous fat layer becomed blurred since they intersect the imaging plane at an oblique angle.

The extent of the interval in the z direction over which material properties are averaged defines the slice thickness. To estimate the slice thickness, a simple 'spiral staircase' model is used. This consists of point scatterers at a series of heights and a series of radii, with the points at each particular height being arranged in one radial direction, forming the steps in the staircase. Fig. 9(a) shows this schematically.

The scatterers are placed at heights of 0-10mm with 0.5mm gaps and radii of 15-50mm with 5mm gaps. Fig. 9(b) is the image obtained with the hybrid method at one position of the array. For an ideal imaging system with 0mm slice thickness the image should contain only a single set of eight scatterers along the radial direction in the plane at $z = 0$. Instead, due

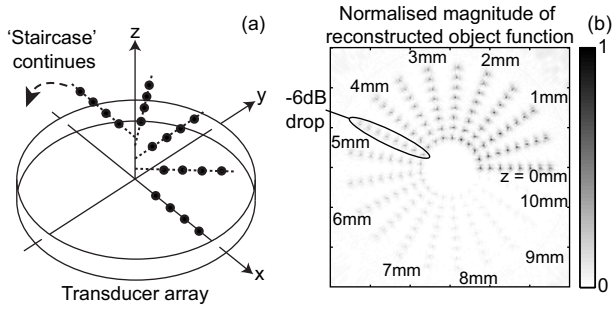

FIG. 9. (a) is a schematic 3D diagram of the arrangement of scatterers in the spiral staircase model. (b) gives the 2D reconstruction of data from such a model, simulated with the 3D FDTD method, for heights 0-10mm at 0.5mm gaps and radii of 15-50mm at 5mm gaps. The artefacts surrounding each scatterer are a result of the relatively course FDTD mesh used, rather than the imaging process, and are ignored. The transducers are modelled as the 12mm tall line sources used in all the simulations in this paper and are at a radius of 60mm. There is a clear drop in response as the height of the scatterer is increased due to the transducer beam height. Following Fig. 8(d), the 4.5mm z offset points lie around the −6dB threshold, indicating this is the boundary of the slice captured by the transducer array.

to the spreading of the PSF in the z direction, weaker reconstructions of the scatterers from different heights can be observed. However, the amplitude of the reconstructed scatterers decays as the corresponding distance from the plane of the array increases. In particular a −6dB drop in amplitude can be observed for the scatterers at $z = 4.5$mm, thus verifying that the slice thickness is around 9mm.

The finite slice thickness is a result of the reduction in sensitivity of the transducer array to scatterers at greater distances from $z = 0$. The sensitivity of the array drops because there is a reduction in both 1) the amplitude of the illuminating beam incident on the scatterer and 2) the sensitivity of the receiving transducer to waves from the scatterer. Here, we consider only a point scatterer along the axis of the array so that the distances to all transducers are the same, and therefore, by the principle of reciprocity, 1) and 2) will both cause the same amplitude drop. Therefore, the −6dB drop in array sensitivity, which

defines the boundary of the slice thickness, will be achieved when the illuminating beam and the receiver sensitivity each drop by −3dB. Considering the Fraunhofer zone of a line transducer[64], the thickness of the beam, B, at the centre of the array with a −3dB threshold as

$$B = \frac{0.884\lambda r_{arr}}{h} \tag{18}$$

where r_{arr} is the radius of the array and h is the transducer height. For the case considered here, the −6dB slice thickness becomes 8.8mm at the centre of the array, which is close enough to the 9mm slice thickness to verify the validity of (18). Equation (18) shows that it is possible that the slice thickness could be reduced by increasing the height of the transducers, although the benefit of this is limited because the Fraunhofer approximation becomes invalid with large transducers. Alternatively, a synthetic aperture approach could be used to reduce the slice thickness as described in Ref. 65.

B. The subtraction problem

The beamforming algorithm in (16) uses the field ψ_δ, which is calculated as the difference between the measured field and the background field

$$\psi_\delta = \psi - \psi_b. \tag{19}$$

However, to obtain the reconstructions in Fig. 5 we have used the total field ψ that is directly available from the measurements in place of ψ_δ. Here, we justify why this is possible.

In principle, ψ_b could be calculated by solving the wave equation with the background field with the FDTD method. However, this would not be reliable in practice because the perturbation field ψ_δ is small compared to ψ and ψ_b, so any small errors in the estimation of ψ_b will cause large errors in ψ_δ. Errors in the ψ_b estimation are unavoidable, mainly because of uncertainty in the transducer response.

Here, we show that it is not necessary to perform the subtraction and it is sufficient to

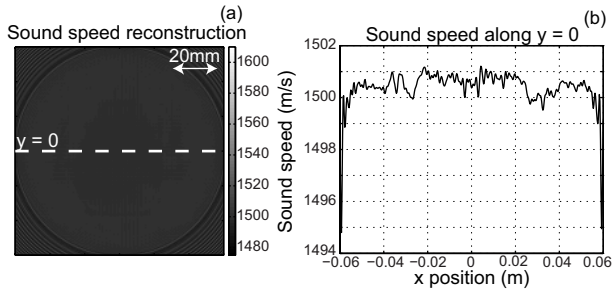

FIG. 10. Image generated by imaging $\psi_\delta = \psi_b$ in the corresponding background velocity field. This is present in the final image if the subtraction is not performed. The error is within ±1m/s through the majority of the imaging domain.

form the BF image from the measured total field directly, i.e.

$$I_\delta(\mathbf{z}) = \int \frac{\psi}{G_b G_b} d\mathbf{x}'. \tag{20}$$

For this purpose it is observed that the BF and filtering steps in HARBUT are linear (for a fixed background) with respect to the measurements. This means that we can define a linear operator, $\mathfrak{I}_{DT}$, that maps the measurements or data, d, onto an image, i, i.e.

$$i = \mathfrak{I}_{DT}(d). \tag{21}$$

When the data correspond to ψ_δ then $O_\delta = \mathfrak{I}_{DT}(\psi_\delta)$. If instead, the data correspond to the total field then

$$\mathfrak{I}_{DT}(\psi) = \mathfrak{I}_{DT}(\psi_\delta) + \mathfrak{I}_{DT}(\psi_b) = O_\delta + \mathfrak{I}_{DT}(\psi_b). \tag{22}$$

The term $\mathfrak{I}_{DT}(\psi_b)$ therefore represents the error caused by making the assumption that the background field does not need to be subtracted. Fig. 10 shows $\mathfrak{I}_{DT}(\psi_b)$ converted to a velocity image for the ψ_b calculated for the TFT background of Fig. 5(b). The velocity map is within ±1m/s of the background except the region outside the array where ring artefacts appear, which is an acceptably small error given that the structures of interest to us have a sound speed contrast relative to the background in the order of 5%.

This convenient property makes the proposed approach very robust because it means that we do not need to estimate ψ_b, thus avoiding significant sources of error.

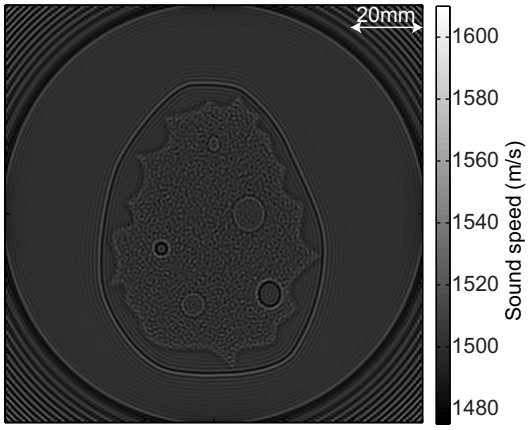

FIG. 11. The artefacts caused by ignoring density variations in the velocity reconstructions. This image is produced from a new 2D simulation. This simulation uses a constant sound speed field of 1500m/s and a density field corresponding to the central slice from Fig. 3. The reconstruction, as with the rest of the paper, assumes density to be negligible and reconstructs the resulting field as velocity perturbations.

C. Density

Here we show that density variations within the breast can be neglected.

Equation (3) defines the object function, which includes a term dependent on the density field. The form of this term means that in order for the density to contribute a significant amount to $O(\mathbf{r})$, a large density gradient must be present. Within soft tissue, density varies continuously; therefore the object function, O, is mainly defined by the sound speed. Even if the density were to vary suddenly at the interface of a cancer mass, the limited density contrast would still make the density term in (3) negligible.

It is possible to isolate the effects of the density field from the velocity field in the reconstruction by performing a new forward simulation with only the density variations present and a constant sound speed. We have performed this simulation in 2D using the central slice from Fig. 3 for the density field. The reconstruction with this data is given in Fig. 11. The sound speed map is obtained assuming that the density term in (3) is negligible. If this were true the reconstructed velocity should be 1500m/s (the same as

the water background) across the image plane, but instead different values of sound speed are seen where density discontinuities occur, showing that density affects the sound speed reconstruction to some extent. However, the values of sound speed significantly differ from the background velocity only at the boundaries of sudden density variations. This leads to two main conclusions: 1) the absolute value of density does not affect the velocity estimate; 2) the errors in velocity at sudden density variations help the visualisation of these boundaries and therefore aid the definition of complex morphologies. It is recognised, however, that density could subsequently be determined from the image by using multiple frequencies according to the approach outlined in Ref. 66.

D. Amplitude correction

The amplitudes of the waves drop as they pass through the 3D breast phantom. One cause of this is the random medium of the glandular region, which scatters energy from the waves in all directions. Some of the energy is scattered out of the plane of the array and is lost; 2D reconstructions ignore this so it becomes a form of attenuation. A second amplitude loss occurs due to the oblique angle at which the wave hits the phantom boundary. The wave is refracted slightly upwards (or downwards depending on the relative sound speeds of the breast and the water) which causes an amplitude drop due to the misalignment of the wave with the receiver[67]. In experimental data both these effects will be present, along with the attenuation caused by the material itself. This loss in amplitude, if it is not accounted for, will cause the reconstructed object function perturbation O_δ to be too small. However, one solution to this problem would be to correct the amplitude loss in the same way we correct the phase. A ray-based attenuation image could be formed in the manner of the TFT image, which would include material attenuation, as well as 3D scattering and deflection since the effects are inseparable. From this, the wave amplitudes at all points in the domain for all illuminations could be calculated using a forward model, which could then correct the Green's functions used in the BF algorithm.

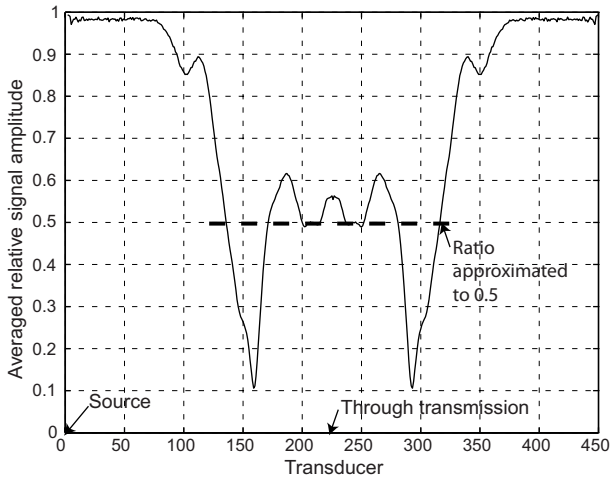

FIG. 12. Amplitude of signal around the array relative to the incident signal at 750kHz. Averaging has been performed across all illuminations by matching up the measurements in the same positions relative to the source. The average amplitude drop of the signal, caused by passing through the phantom, was taken to be 0.5.

By taking the measurements of Fig. 4(b), dividing by the equivalent incident field (i.e. the field corresponding to a unit point source as defined by $G_w(\mathbf{x}, \mathbf{y})$), and averaging for the positions around the array relative to the source, Fig. 12 can be produced. This gives an estimate of how the amplitude drops through the breast due to the factors discussed above. We make the assumption that this amplitude drop can be corrected in our image by multiplying O_δ by a constant factor. From Fig. 12, we estimate the necessary factor to be 2 since the transmitted signals' amplitudes drop, on average, by a factor of 0.5 or 6dB.

Our simulations do not model attenuation. We can estimate the effect of this by assuming that attenuation through the breast is around 0.75dB/cm/MHz[57], leading to a typical amplitude drop across the breast of less than 3dB. This would add a small contribution to the overall amplitude drop and could be accounted for through the compensation technique described above.

VII. CONCLUSIONS

We have introduced HARBUT, the Hybrid Algorithm for Robust Breast Ultrasound Tomography, which provides a resolution improvement over Time-of-Flight Tomography while avoiding the convergence and speed problems of iterative methods. Diffraction Tomography methods are unsuitable for this purpose because the contrast and size of the breast relative to the homogeneous water background breaks the Born approximation. By reformulating the problem using an inhomogeneous background which is sufficiently close to the actual sound speed map, the relative contrast can be reduced such that the approximation becomes valid.

It is shown that the TFT algorithm can provide such a background. Imaging against this is performed in two stages. A modified BF algorithm, using Green's functions calculated for the background, generates the first image. This is then converted into the equivalent DT image by filtering in the spatial frequency domain.

HARBUT is demonstrated to accurately reconstruct the sound speed through a breast phantom model from 3D simulated data, despite sampling the wavefield with an array architecture suitable for 2D imaging, and the presence of uncertainties such as transducer response that are likely to occur in real experiments. At a frequency of 750kHz, masses as small as 4mm in diameter can be clearly imaged. An in-plane resolution of 1mm was achieved, with a slice thickness of 9mm. Density contrast and randomly varying material properties with sub-wavelength coherence lengths have little influence on the final reconstruction. 3D structures intersecting the plane of the array are partially projected onto the imaging plane due to the size of the slice thickness.

Acknowledgments

The authors would like to thank EPSRC for supporting this research with grant EP/F00947X/1.

References

[1] F. Kamangar, G. Dores, and W. Anderson, "Patterns of cancer incidence, mortality, and prevalence across five continents: defining priorities to reduce cancer disparities in different geographic regions of the world", Journal of Clinical Oncology **24**, 2137 (2006).

[2] P. Autier, M. Boniol, C. LaVecchia, L. Vatten, A. Gavin, C. Hery, and M. Heanue, "Disparities in breast cancer mortality trends between 30 european countries: retrospective trend analysis of who mortality database", British Medical Journal **341**, 3620 (2010).

[3] M. Silverstein, M. Lagios, A. Recht, D. Allred, S. Harms, R. Holland, D. Holmes, L. Hughes, R. Jackman, T. Julian, *et al.*, "Image-detected breast cancer: state of the art diagnosis and treatment", Journal of the American College of Surgeons **201**, 586–597 (2005).

[4] T. M. Kolb, J. Lichy, and J. H. Newhouse, "Comparison of the performance of screening mammography, physical examination, and breast us and evaluation of factors that influence them: An analysis of 27,825 patient evaluation", Radiology **225**, 165–175 (2002).

[5] P. C. Stomper, D. J. D'Souza, P. A. Dinitto, and et al., "Analysis of parenchymal density on mammograms in 1353 women 25-79 years old", AJR Am J Roentgenol **167**, 1261–1265 (1996).

[6] D. Saslow, C. Boetes, W. Burke, S. Harms, M. Leach, C. Lehman, E. Morris, E. Pisano, M. Schnall, S. Sener, *et al.*, "American cancer society guidelines for breast screening with mri as an adjunct to mammography", CA: A Cancer Journal for Clinicians **57**, 75 (2007).

[7] M. Kriege, C. Brekelmans, C. Boetes, P. Besnard, H. Zonderland, I. Obdeijn, R. Manoliu, T. Kok, H. Peterse, M. Tilanus-Linthorst, *et al.*, "Efficacy of mri and mammography for breast-cancer screening in women with a familial or genetic predisposition", The New England journal of medicine **351**, 427 (2004).

[8] J. F. Greenleaf, S. A. Johnson, S. L. Lee, G. T. Herman, and E. H. Wood, "Algebraic reconstruction of spatial distributions of acoustic absorption within tissue from their two-dimensional acoustic projections", International Symposium on Acoustical Holography

and Imaging, 5th, Palo Alto, Calif **5**, 591–603 (1973).

[9] P. Carson, C. Meyer, A. Scherzinger, and T. Oughton, "Breast imaging in coronal planes with simultaneous pulse echo and transmission ultrasound", Science **214**, 1141 (1981).

[10] J. Schreiman, J. Gisvold, J. Greenleaf, and R. Bahn, "Ultrasound transmission computed tomography of the breast", Radiology **150**, 523 (1984).

[11] M. P. Andre, H. S. Janee, P. Martin, G. P. Otto, B. A. Spivey, and D. A. Palmer, "High-speed data acquisition in a diffraction tomography system employing large-scale toroidal arrays", Int. J. Imag. Syst. Tech. **8**, 137–147 (1997).

[12] N. Duric, P. Littrup, L. Poulo, A. Babkin, R. Pevzner, E. Holsapple, O. Rama, and C. Glide, "Detection of breast cancer with ultrasound tomography: First results with the computed ultrasound risk evaluation (cure) prototype", Medical physics **34**, 773 (2007).

[13] H. Gemmeke and N. Ruiter, "3d ultrasound computer tomography for medical imaging", Nuclear Instruments and Methods in Physics Research Section A: Accelerators, Spectrometers, Detectors and Associated Equipment **580**, 1057–1065 (2007).

[14] S. Mensah and E. Franceschini, "Near-field ultrasound tomography", J. Acoust. Soc. Am. **121**, 1423–33 (2007).

[15] C. Hansen, N. Huttebrauker, H. Ermert, M. Hollenhorst, L. Heuser, and G. Schulte-Altedorneburg, "Determination of a mean sound velocity in the female breast for artifact reduction in full angle spatial compounding", in *Ultrasonics Symposium (IUS), 2009 IEEE International*, 538–541 (IEEE) (2010).

[16] J. F. Greenleaf, S. A. Johnson, W. F. Samayoa, and F. A. Duck, "Algebraic reconstruction of spatial distributions of acoustic velocities in tissue from their time-of-flight profiles", in *Acoustical Holography*, edited by P. S. Green, volume 6, 71–90 (Plenum Press, New York) (1975).

[17] J. Greenleaf, S. Johnson, and R. Bahn, "Quantitative cross-sectional imaging of ultrasound parameters", in *Ultrasonics Symposium, 1977*, 989–995 (1977).

[18] H. Schomberg, "An improved approach to reconstructive ultrasound tomography", Journal of Physics D: Applied Physics **11**, L181 (1978).

[19] M. Krueger, A. Pesavento, and H. Ermert, "A modified time-of-flight tomography concept for ultrasonic breast imaging", IEE Ultrasonics Symposium 1381–1385 (1996).

[20] Y. Quan and L. Huang, "Sound-speed tomography using first-arrival transmission ultrasound for a ring array", in *Proc. SPIE*, volume 6513, pp. 651306-1–651306-9 (2007).

[21] S. Li, M. Jackowski, D. Dione, T. Varslot, L. Staib, and K. Mueller, "Refraction corrected transmission ultrasound computed tomography for application in breast imaging", Medical Physics **37**, 2233 (2010).

[22] A. Hormati, I. Jovanovic, O. Roy, and M. Vetterli, "Robust ultrasound travel-time tomography using the bent ray model", in *Society of Photo-Optical Instrumentation Engineers (SPIE) Conference Series*, volume 7629, pp. 76290I-1–76290I-12 (2010).

[23] K. Tanabe, "Projection method for solving a singular system of linear equations and its applications", Numerische Mathematik **17**, 203–214 (1971).

[24] A. Louis and F. Natterer, "Mathematical problems of computerized tomography", Proceedings of the IEEE **71**, 379–389 (1983).

[25] P. Williamson, "A guide to the limits of resolution imposed by scattering in ray tomography", Geophysics **56**, 202–207 (1991).

[26] R. Snieder and A. Lomax, "Wavefield smoothing and the effect of rough velocity perturbations on arrival times and amplitudes", Geophysical Journal International **125**, 796–812 (1996).

[27] G. Schuster, "Resolution limits for crosswell migration and traveltime tomography", Geophysical Journal International **127**, 427–440 (1996).

[28] R. Pratt, "Seismic waveform inversion in the frequency domain, part 1: Theory and verification in a physical scale model", Geophysics **64**, 888–901 (1999).

[29] P. Thore and C. Juliard, "Fresnel zone effect on seismic velocity resolution", Geophysics **64**, 593–603 (1999).

[30] S. Hung, F. Dahlen, and G. Nolet, "Wavefront healing: a banana–doughnut perspective", Geophysical Journal International **146**, 289–312 (2001).

[31] J. Spetzler, C. Sivaji, O. Nishizawa, and Y. Fukushima, "A test of ray theory and scat-

tering theory based on a laboratory experiment using ultrasonic waves and numerical simulation by finite-difference method", Geophysical Journal International **148**, 165–178 (2002).

[32] A. Devaney, "A filtered backpropagation algorithm for diffraction tomography", Ultrasonic imaging **4**, 336–350 (1982).

[33] M. Born and E. Wolf, *Principles of Optics* pp. 695–703 (Cambridge University Press, Cambridge) (1999).

[34] A. C. Kak and M. Slaney, *Principles of computerized tomographic reconstruction* pp. 203–218 (IEEE Press, New York) (1998).

[35] F. Simonetti, L. Huang, N. Duric, and P. Littrup, "Diffraction and coherence in breast ultrasound tomography: A study with a toroidal array", Medical physics **36**, 2955 (2009).

[36] F. Natterer and F. Wubbeling, *Mathematical methods in image reconstruction* pp. 1–216 (Society for Industrial Mathematics) (2001).

[37] A. Tarantola, *Inverse problem theory and methods for model parameter estimation* pp. 1–630(Society for Industrial Mathematics) (2005).

[38] J. Wiskin, D. Borup, S. Johnson, M. Berggren, T. Abbott, and R. Hanover, "Full-wave, non-linear, inverse scattering", Acoustical Imaging 183–193 (2007).

[39] T. D. Mast, "Aberration correction for time-domain ultrasound diffraction tomography", The Journal of the Acoustical Society of America **112**, 55 (2002).

[40] P. M. Morse and K. U. Ingard, *Theoretical Acoustics*, pp. 227–305 (McGraw-Hill Book Company, New York, London) (1968).

[41] S. Pourjavid and O. Tretiak, "Numerical solution of the direct scattering problem through the transformed acoustical wave equation", The Journal of the Acoustical Society of America **91**, 639 (1992).

[42] W. Chew and Y. Wang, "Reconstruction of two-dimensional permittivity distribution using the distorted born iterative method", IEEE Transactions on Medical Imaging **9**, 218–225 (1990).

[43] F. Simonetti and L. Huang, "From beamforming to diffraction tomography", Journal of

Applied Physics **103**, 103110 (2008).

[44] S. Norton and M. Linzer, "Ultrasonic reflectivity imaging in three dimensions: exact inverse scattering solutions for plane, cylindrical, and spherical apertures.", IEEE transactions on bio-medical engineering **28**, 202 (1981).

[45] F. Anderson and F. Morgan, "Active imaging analysis via ellipsoidal projections", Acoustical imaging **21**, 171–182 (1995).

[46] J. Jensen, S. Nikolov, K. Gammelmark, and M. Pedersen, "Synthetic aperture ultrasound imaging", Ultrasonics **44**, e5–e15 (2006).

[47] S. Li, K. Mueller, M. Jackowski, D. Dione, and L. Staib, "Fast marching method to correct for refraction in ultrasound computed tomography", in *3rd IEEE International Symposium on Biomedical Imaging: Nano to Macro, 2006*, 896–899 (2006).

[48] J. Sethian, "A fast marching level set method for monotonically advancing fronts", Proceedings of the National Academy of Sciences of the United States of America **93**, 1591 (1996).

[49] W. Schneider, "Integral formulation for migration in two and three dimensions", Geophysics **43**, 49 (1978).

[50] M. Haynes and M. Moghaddam, "Large-domain, low-contrast acoustic inverse scattering for ultrasound breast imaging", Biomedical Engineering, IEEE Transactions on **57**, 2712–2722 (2010).

[51] T. D. Mast, "Wideband quantitative ultrasonic imaging by time-domain diffraction tomography", The Journal of the Acoustical Society of America **106**, 3061 (1999).

[52] C. Li, N. Duric, P. Littrup, and L. Huang, "In vivo breast sound-speed imaging with ultrasound tomography", Ultrasound in medicine & biology **35**, 1615–1628 (2009).

[53] S. Goss, R. Johnston, and F. Dunn, "Comprehensive compilation of empirical ultrasonic properties of mammalian tissues", The Journal of the Acoustical Society of America **64**, 423 (1978).

[54] E. Franceschini, S. Mensah, D. Amy, and J. Lefebvre, "A 2-d anatomic breast ductal computer phantom for ultrasonic imaging", IEEE transactions on ultrasonics, ferroelectrics,

and frequency control **53**, 1281 (2006).

[55] L. Foldy, "The multiple scattering of waves. i. general theory of isotropic scattering by randomly distributed scatterers", Physical Review **67**, 107–119 (1945).

[56] M. Cowan, K. Beaty, J. Page, Z. Liu, and P. Sheng, "Group velocity of acoustic waves in strongly scattering media: Dependence on the volume fraction of scatterers", Physical Review E **58**, 6626–6636 (1998).

[57] T. D. Mast, "Empirical relationships between acoustic parameters in human soft tissues", Acoustics Research Letters Online **1**, 37 (2000).

[58] F. Simonetti, L. Huang, and N. Duric, "On the sampling of the far-field operator with a circular ring array", J. Appl. Phys. **101**, 083103 (2007).

[59] K. Yee, "Numerical solution of inital boundary value problems involving maxwell's equations in isotropic media", IEEE Transactions on antennas and propagation **14**, 302–307 (1966).

[60] D. Komatitsch and R. Martin, "An unsplit convolutional perfectly matched layer improved at grazing incidence for the seismic wave equation", Geophysics **72**, 155–167 (2007).

[61] N. Wiener, *Extrapolation, interpolation, and smoothing of stationary time series* pp. 1–116 (The MIT Press) (1964).

[62] C. Li, L. Huang, N. Duric, H. Zhang, and C. Rowe, "An improved automatic time-of-flight picker for medical ultrasound tomography", Ultrasonics **49**, 61–72 (2009).

[63] A. Goldstein and B. Madrazo, "Slice-thickness artifacts in gray-scale ultrasound", Journal of Clinical Ultrasound **9**, 365–375 (1981).

[64] J. W. Goodman, *Introduction to Fourier Optics* pp. 73–75 (McGraw-Hill, New York) (1996).

[65] F. Simonetti and L. Huang, "Synthetic aperture diffraction tomography for three-dimensional imaging", Proceedings of the Royal Society A: Mathematical, Physical and Engineering Science **465**, 2877 (2009).

[66] R. Lavarello and M. Oelze, "Density imaging using inverse scattering", The Journal of

the Acoustical Society of America **125**, 793 (2009).

[67] F. Simonetti, L. Huang, and N. Duric, "A multiscale approach to diffraction tomography of complex three-dimensional objects", Appl. Phys. Lett. **95**, 061904 (2009).

TABLE I. Material properties of the structures in the breast phantom

Structure	**Sound speed (m/s)**	**Density (kg/m^3)**	**Standard deviation (%)**	**Correlation length (mm)**
Water	1500	1000	-	-
Glandular region	1550	1060	2	1.5
Fat	1470	950	-	-
Cancer masses	1580	1100	1	1.5

TABLE II. Dimensions of the inclusions in the breast phantom. Inclusion numbering is performed clockwise from the top as shown in Fig. 3.

Inclusion Number	**Location (mm)**			**Diameter (mm)**			**Type**
	x	**y**	**z**	**x**	**y**	**z**	
1	0	-20	0	3	4	4	Cancer
2	10	0	0	9	10	9	Cancer
3	16	23	-1	7	8	8	Fat sphere
4	-6	26	1	7	7	7	Cancer
5	-15	10	0	4	4	4	Fat sphere

TABLE III. Reconstructed average sound speeds within each inclusion

Inclusion	**Actual sound speed (m/s)**	**Reconstructed sound speed (m/s)**	**Error**
1	1580	1568	0.76%
2	1580	1575	0.32%
3	1470	1463	0.48%
4	1580	1571	0.57%
5	1470	1473	0.20%

List of Figures